(Supplementary Information)

High temperature stability in few atomic layer MoS_2 based thin film heterostructures: Structural, static and dynamic magnetization properties

Nanhe Kumar Gupta[1], Amar Kumar[1], Lalit Pandey[1], Soumyarup Hait[1$], Vineet Barwal[1,#], Amir Khan[1], Vireshwar Mishra[1], Nikita Sharma[1], Nakul Kumar[1], and Sujeet Chaudhary[1]*

[1]*Thin Film Laboratory, Department of Physics, Indian Institute of Technology Delhi, New Delhi 110016, India*

[$] *Present address: School of Electrical and Electronic Engineering, Nanyang Technological University, Singapore,639798*

[#]*Present address: Centre for Magnetic and Spintronic Materials (CMSM), National Institute for Materials Science (NIMS) 1-2-1 Sengen, Tsukuba, Ibaraki 305-0047, Japan*

sujeetc@physics.iitd.ac.in,

1 Thin film deposition systems:

The bilayer heterostructures of $MoS_2/Co_{60}Fe_{20}B_{20}$ (CoFeB) were deposited on Thermally oxidised Si(100) substrates at room temperature (RT) using high vacuum pulsed-direct current (DC) magnetron sputtering system [Make: *Excel Instruments*, India]. The cross-sectional schematic and interior view of DC sputtering system shown in figure S1(a). Prior to the deposition, the base pressure of the sputtering chamber was maintained at 3×10^{-8} Torr with *turbomolecular* and *rotary vane* pumps. The films were deposited at a working pressure of 1.1×10^{-3} Torr, which was maintained by flowing Argon gas at 15 sccm. Prior to the deposition, the Si/SiO_2(300 nm) substrates were cleaned using standard chemical processes. All the films were deposited at room temperature (RT) in quick succession using the load lock equipped with growth chamber. The growth rates of individuals targets were precisely calibrated. At left side upper panel in figure S1 shows the thin film stack while at lower panel in left side depicts the photograph of plasma during sputtering. Schematic of sulfurization system, which was used to grow MoS_2 films. Figure S1(c) illustrates the photograph from inside chamber during operation H_2S/Ar Plasma.

Growth methodology of MoS_2: Further, for the growth of MoS_2, Mo films of different nominal thicknesses were first grown on thermally oxidized Si(100) substrates at RT using the same *Excel Instrument India* make magnetron sputtering system. The thickness of the Mo films is precisely controlled by maintaining a very low deposition rate (0.20 Å/s). The as-deposited Mo

ultrathin films were then transferred to another high vacuum chamber for the plasma-sulfurization process (for MoS_2 synthesis- schematic of sulphurisation chamber shown in figure S1(b)). The grown Mo films were kept on a Mo boat and heated to a temperature of ~ 450ºC. A gas mixture of H_2S (10%) mixed with Ar (90%) was fed to the chamber followed by maintaining the pressure at ~0.65 Torr. After that, A stable intense plasma was generated by applying a voltage of 1 kV across two cylindrical-shaped Aluminium electrodes as shown in figure S1(c). The distance between the electrodes was ~7.5 cm. The sulfurization process was continued for 1 hour, and after completing the sulphurisation process, the power to the electrodes and H_2S gas source were switch off simultaneously. Then the samples were cooled down to RT in a pure Ar gas environment at a pressure of ~0.90 Torr. More details of the sulfurization process can be found in the published reports [1,2]. After completing the sulfurization process, the samples were transferred back to the sputtering chamber for the growth of the CoFeB layer and the Al capping layer of the heterostructures. Prior to the deposition of CoFeB and Al layer, the grown MoS_2 layer was thermally treated in the sputtering chamber at 200°C for 1.5 hours to get rid of any impurities/contamination if formed during the transferring of the MoS_2 coated substrate from the sulfurization chamber. The details of the growth /sputtering parameters used for the deposition of CoFeB, Mo and Al are listed in Table S1

Table S1: Growth parameters used for the depositing the individual layers in the heterostructures.

Sputtering conditions	CoFeB	Mo	Al
Pulsed DC Power	140 W	15 W	30 W
Gas flow	15 sccm	15 sccm	15 sccm
Base Pressure	~3×10^{-8} Torr	~3×10^{-8} Torr	~3×10^{-8} Torr
Working Pressure	1.1×10^{-3} Torr	1.1×10^{-3} Torr	1.1×10^{-3} Torr
Target to substrate distance	~11 cm	~11 cm	~11 cm
Growth temperature	300 K	300 K	300 K
Growth rate	1.42 $\text{Å}/s$	0.20 $\text{Å}/s$	0.42 $\text{Å}/s$

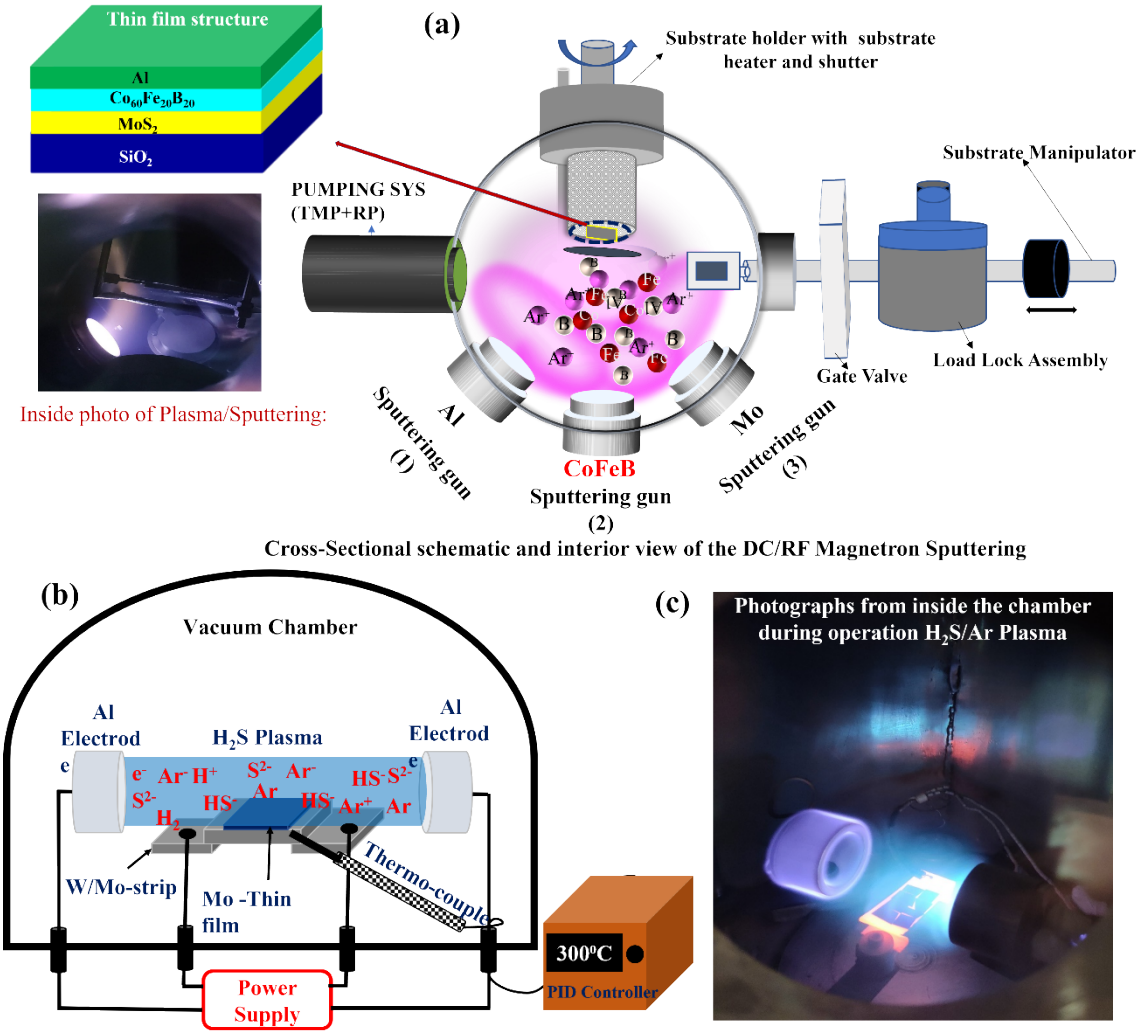

Figure S1: (a) Cross-section schematic and interior view of employed RF/DC magnetron sputtering system equipped with *turbomolecular pump* (TMP) and *rotary vane pump* (RP). In left side upper panel depicts the thin film stack/heterostructures and lower panel shows inside photo of plasma during sputtering. (b) Schematics of experimental set-up for utilising H_2S/Ar plasma(c) Real photographs of plasma assisted sulfurization (H_2S/Ar Plasma) processes.

2 Elemental energy dispersive X-ray mapping:

Energy dispersive spectroscopy (EDS) spectroscopy was performed on a selected sample of series TMD1. The measurement was performed over a scan area of 400 × 400 μm^2 with electron beam of energy 15 keV to ascertain the compositional homogeneity in the grown films.

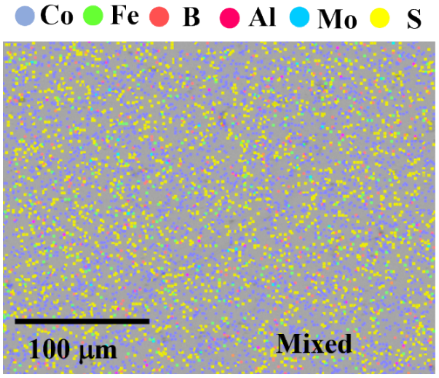

Figure S2: Combined EDS maps of (a) MoS_2 (ML)/CoFeB(8nm)/Al(4nm).The filled circles with different colour *i.e.*, sky blue, green, light maroon, pink, navy blue and yellow represent the atoms of Co, Fe, B, Al, Mo and S, respectively.

The EDS maps of the sample shown in figure B1 reveals the compositional homogeneity in the growth of the layers even in a few atomically thick layers of MoS_2 $\{(^{n_L = 1 \;\; i.e.,\; 0.83\; nm}\}$.

3 Static magnetization analysis:

Magnetization hysteresis loops of the select samples of series TMD1{MoS_2(ML)/ CoFeB (4nm) and MoS_2(ML)/ CoFeB (8nm)}, and TMD1A {MoS_2(ML)/ CoFeB (4nm) and MoS_2(ML)/ CoFeB (8nm)} are shown in figure S3. The calculated value of M_s is discussed in manuscript.

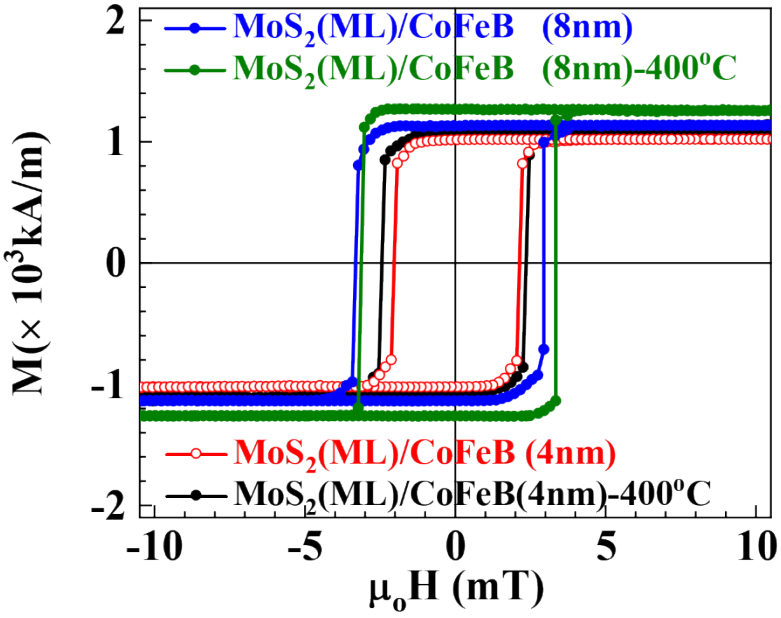

Figure S3: M-H hysteresis loops of some of the representative t samples of the different series: TMD1{MoS_2(ML)/CoFeB(4nm) and MoS_2(ML)/CoFeB(8nm)} and TMD1A {MoS_2(ML)/CoFeB(4nm) and MoS_2(ML)/CoFeB(8nm)}.

4 Ferromagnetic resonance:

The dynamic magnetization response was recorded using a home-built broadband ferromagnetic resonance (FMR) set up equipped with Vector Network Analyzer (VNA) *[Model: 8719ES, make: HP],* an electromagnet, Helmholtz coil, bipolar power supply (*Model: BOP 36-12 DL, make: KEPCO*), digital Gauss meter (*Model: 455 DSP, make: Lakeshore;*) and a co-planar waveguide (CPW) based transmission line [3]. The samples were placed facing the CPW and the frequency (*f*) range of $4-12$ GHz was used to record the FMR spectra. For a given (fixed) excitation frequency of the microwave power (0 dBm or 1mW) and field (0.03 mT) applied perpendicular to the dc field ($\mu_0 H_{eff}$) and along the film surface, the external magnetic field (higher than the saturation field) was swept to track the resonance condition. For efficiently detecting the absorbed microwave signal, the external field $\mu_0 H_{eff}$ is modulated by applying an ac magnetic field ($\mu_0 h_{rf}$) of 0.13 mT at 211.5 Hz, generated by powering a pair of Helmholtz coils from the oscillator output of a Lock-in amplifier (LIA) *[Model: SR 830, make: Stanford Research Systems Inc.]*, which also detected the FMR signal [1].

It may be pointed out that while for a single FM layer, the α_{eff} basically represents the relaxation of spin angular momentum within the FM lattice predominantly due to the intrinsic magnon-electron scattering mechanism [4], but when a NM is placed adjacent to the FM, a part of the net spin angular momentum also gets transferred (spin pumped) into the adjacent NM (here, MoS_2) layer, which results in an enhancement in the overall damping which is indicated by α_{eff} as shown in figure S4(a) for the samples of TMD2 and TMD2A series, respectively.

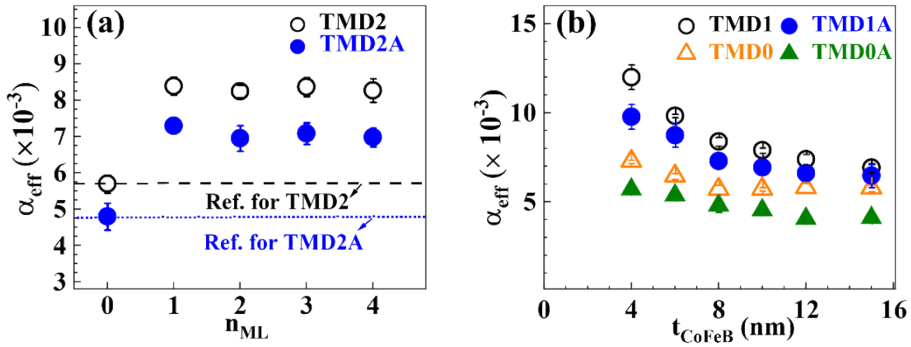

Figure S4: (a) Variation in the effective damping (α_{eff}) as a function of n_{ML} for all the samples from the TMD2 and TMD2A series. The two dashed lines in black and blue colour depict the effective damping of the as-grown CoFeB (8nm)/Al(4nm) sample of TMD0-series and the annealed CoFeB (8nm)/Al(4nm) sample from TMD0A-series, respectively. These represent the reference for TMD2 and TMD2A series samples, respectively. (b) Variation in effective damping

constant with t_{CoFeB} for various samples of the TMD0, TMD0A, TMD1 and TMD1A, series respectively.

Now, we turn to the effect of ferromagnetic thickness on one of the most important dynamic magnetization response parameters, *i.e.*, α_{eff} in these MoS_2/CoFeB heterostructures. Figure S4(b) show the variation of α_{eff} on the t_{CoFeB} for samples of the TMD0, TMD0A, TMD1 and TMD1A series. It can be seen that the α_{eff} values are significantly higher for the samples of TMD1 and TMD1A series compared to that those from the TMD0 (which does not contain MoS_2) and TMD0A (which also does not contain MoS_2, for the 400°C/1 hour annealed) series, respectively. This improved effective damping in the samples of TMD1 and TMD1A series is attributed to the spin pumping to the MoS_2.

5 DFT calculations: computational details and results:

As discussed in manuscript, the spin pumping in CoFeB/TMD heterostructure depends upon the number of TMD layers, density of states (DOS) and spin orbit coupling (SOC) strength near the Fermi level. Thus, we briefly summarize the main features of the MoS_2 multilayers' energy bands without and with SOC consideration. DFT calculations were carried out using the QUANTUM ESPRESSO code[5,6].We used generalized gradient approximation (GGA) proposed by Perdew-Burke-Ernzerh (PBE) to approximate the electronic exchange and correlation interactions[7]. The projector augment wave pseudopotential from PSlibrary with valence electronic configuration of Mo ($4s^2 5s^1 4p^6 4d^5$) and S ($3s^2 3p^4$) are used [8]. A 11×11×1 sized Monkhorst-Pack grid is considered for the k-points sampling, and the cut-off energy for the plane waves is chosen to be 200 Ry for all calculations. The convergence thresholds for the self-consistent cycle energy are set to 10^{-6} Ry. The multilayer MoS_2 slabs with different numbers of layers ranging from one monolayer to four layers (ML, 2L, 3L and 4L) are modelled along the [001] direction of MoS_2 bulk structure since the van der Waals interaction between MoS_2 layers is along the [001] direction. The mono- and multi-layered MoS_2 slabs are modelled with a vacuum spacing of 20 Å in the Z-direction to prevent interactions between adjacent MoS_2 slabs and with all different possible terminations viz; MoS, SS, and SMo terminations. Figures S5 (a-c) show the schematic for MoS_2 - 4L with different above-mentioned terminations used in calculations. In order to achieve the minimum energy state for all multilayer slabs, the atomic positions were allowed to relax until the total force on atoms was less than the 10^{-3} Ry/Bohr. Table S2 tabulated the total energy of the relaxed mono and multi-layered slabs which indicated that all the slabs are stable as all have negative total energy. Also,

the slabs with MoS terminations have the lowest energy among all the terminations for mono- and all multi-layer's slab. The optimized plane structural parameters of the monolayer and all multilayers are similar to those of the bulk case (see Table S3).

Table S2: The total energy for the relaxed structures with different numbers of layers and different terminations without inclusions of SOC(WO/SOC) and with SOC

Energy		**Mo-S termination**	**S-Mo termination**	**S-S termination**
Monolayer	WO/SOC	-496.70 eV	-496.32 eV	-496.32 eV
	SOC	-497.16 eV	-496.84 eV	-496.79 eV
Bilayer	WO/SOC	-993.40 eV	-993.02 eV	-993.01 eV
	SOC	-994.31 eV	-994.07 eV	-994.14 eV
Trilayer	WO/SOC	-1490.09 eV	-1489.70 eV	-1489.70 eV
	SOC	-1491.46 eV	-1491.34 eV	-1491.34 eV
Tetralayer	WO/SOC	-1986.79 eV	-1986.40 eV	-1986.40 eV
	SOC	-1988.61 eV	-1988.76 eV	-1988.34 eV

Table S3: Geometrical parameters, bandgaps without (WO) and with SOC considerations for bulk, ML, 2L, 3L and 4L MoS_2 using GGA functional.

n_L	**Lattice constant of MoS_2**	**Band gap**	
		Without SOC	**With SOC**
ML	a = b =3.16 Å, c = 23.08 Å	1.73 eV	1.65 eV
2L	a = b = 3.20 Å, c = 30.06 Å	1.37 eV	1.35 eV
3L	a = b = 3.20 Å, c = 37.01 Å	1.29 eV	1.28 eV
4L	a = b = 3.20 Å, c = 43.96 Å	1.28 eV	1.26 eV
Bulk	a = b = 3.20 Å, c = 13.89 Å (a=b = 3.18 Å, c = 13.83 Å) [9] (a=b = 3.19Å, c = 12.41 Å) [10]	1.24 eV	1.22 eV

The lattice constants of bulk MoS_2 are calculated to be a = b = 3.20 Å, c = 13.89 Å, which are alike to the other reported values[9,10]. In the unit cell of MoS_2, two Molybdenum atoms are positioned at (0.66, 0.33, 0.75) and (0.33, 0.66, 0.25), while four Sulphur atoms are positioned at (0.66, 0.33, 0.64), (0.33, 0.66, 0.14), (0.33, 0.66, 0.36) and (0.66, 0.33, 0.86) respectively.

Based on the optimized slab structures, the band structures and density of states were further calculated and analysed. The band structure and density of states plot for 2 L and 3L MoS_2 are shown in figure S5 (c, d, e & f), and band gap values for mono- and multi-layers with and without SOC are listed in Table S3.

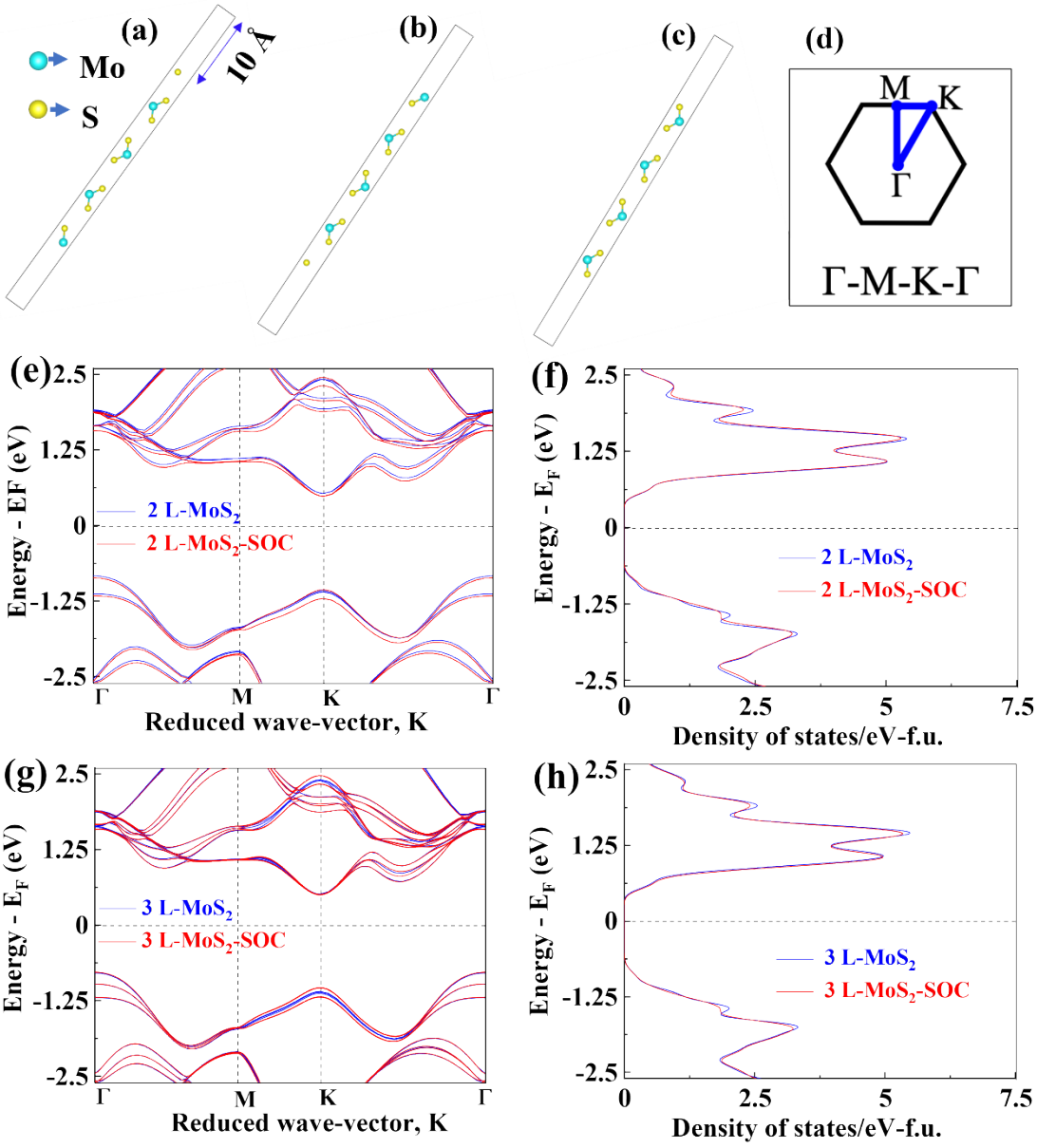

Figure S5: Schematic for MoS_2 4L with (a) Mo-S termination, (b) S-S termination, (c) S-Mo termination and (d) k-point path for band structure calculations for 1ML, 2ML, 3ML and 4ML- MoS_2. (e), (g), band structure and (f) and (h) density of states plot for MoS_2 –2L and 3L, respectively. Blue and Red solid lines correspond to the bands/DOS without and with SOC, respectively. Fermi level is set at 0 eV

References:

1 S. Hait, S. Husain, V. Barwal, N. K. Gupta, L. Pandey, P. Svedlindh and S. Chaudhary, *J. Magn. Magn. Mater.*, 2021, **519**, 167509.

2 S. Husain, A. Kumar, P. Kumar, A. Kumar, V. Barwal, N. Behera, S. Choudhary, P. Svedlindh and S. Chaudhary, *Phys. Rev. B*, 2018, **98**, 180404.

3 N. Behera, IIT Delhi, 2017.

4 K. Gilmore, Y. U. Idzerda and M. D. Stiles, *J. Appl. Phys.*, 2008, **103**, 07D303.

5 P. Giannozzi, O. Andreussi, T. Brumme, O. Bunau, M. Buongiorno Nardelli, M. Calandra, R. Car, C. Cavazzoni, D. Ceresoli, M. Cococcioni, N. Colonna, I. Carnimeo, A. Dal Corso, S. de Gironcoli, P. Delugas, R. A. Distasio, A. Ferretti, A. Floris, G. Fratesi, G. Fugallo, R. Gebauer, U. Gerstmann, F. Giustino, T. Gorni, J. Jia, M. Kawamura, H.-Y. Y. Ko, A. Kokalj, E. Kücükbenli, M. Lazzeri, M. Marsili, N. Marzari, F. Mauri, N. L. Nguyen, H.-V. V. Nguyen, A. Otero-de-la-Roza, L. Paulatto, S. Poncé, D. Rocca, R. Sabatini, B. Santra, M. Schlipf, A. P. Seitsonen, A. Smogunov, I. Timrov, T. Thonhauser, P. Umari, N. Vast, X. Wu, S. Baroni, E. Küçükbenli, M. Lazzeri, M. Marsili, N. Marzari, F. Mauri, N. L. Nguyen, H.-V. V. Nguyen, A. Otero-de-la-Roza, L. Paulatto, S. Poncé, D. Rocca, R. Sabatini, B. Santra, M. Schlipf, A. P. Seitsonen, A. Smogunov, I. Timrov, T. Thonhauser, P. Umari, N. Vast, X. Wu and S. Baroni, *J. Phys. Condens. Matter*, 2017, **29**, 465901.

6 P. Giannozzi, S. Baroni, N. Bonini, M. Calandra, R. Car, C. Cavazzoni, D. Ceresoli, G. L. Chiarotti, M. Cococcioni, I. Dabo, A. Dal Corso, S. de Gironcoli, S. Fabris, G. Fratesi, R. Gebauer, U. Gerstmann, C. Gougoussis, A. Kokalj, M. Lazzeri, L. Martin-Samos, N. Marzari, F. Mauri, R. Mazzarello, S. Paolini, A. Pasquarello, L. Paulatto, C. Sbraccia, S. Scandolo, G. Sclauzero, A. P. Seitsonen, A. Smogunov, P. Umari and R. M. Wentzcovitch, *J. Phys. Condens. Matter*, 2009, **21**, 395502.

7 J. P. Perdew, K. Burke and M. Ernzerhof, *Phys. Rev. Lett.*, 1996, **77**, 3865–3868.

8 A. Dal Corso, *Comput. Mater. Sci.*, 2014, **95**, 337–350.

9 P. Johari and V. B. Shenoy, *ACS Nano*, 2011, **5**, 5903–5908.

10 J. Q. Hu, X. H. Shi, S. Q. Wu, K. M. Ho and Z. Z. Zhu, *Nanoscale Res. Lett.*, 2019, **14**, 1–13.